Bjoern F. Klose[1]
Institute of Test and Simulation for Gas Turbines
German Aerospace Center (DLR)
Linder Höhe, 51147 Cologne, Germany
email: bjoern.klose@dlr.de

Christian Morsbach
Institute of Propulsion Technology
German Aerospace Center (DLR)
Linder Höhe, 51147 Cologne, Germany

Michael Bergmann
Institute of Propulsion Technology
German Aerospace Center (DLR)
Linder Höhe, 51147 Cologne, Germany

Edwin J. Munoz Lopez
Institute of Propulsion Technology
German Aerospace Center (DLR)
Linder Höhe, 51147 Cologne, Germany

Alexander Hergt
Institute of Propulsion Technology
German Aerospace Center (DLR)
Linder Höhe, 51147 Cologne, Germany

Edmund Kügeler
Institute of Propulsion Technology
German Aerospace Center (DLR)
Linder Höhe, 51147 Cologne, Germany

The Unsteady Shock-Boundary Layer Interaction in a Compressor Cascade – Part 2: High-Fidelity Simulation

In the second part of this three-paper series, high-fidelity simulations of the Transonic Cascade TEAMAero at the aerodynamic design point with $\mathrm{Re}_{\mathrm{in}} = 1.35{\times}10^6$ *and* $\mathrm{Ma}_{\mathrm{in}} = 1.21$ *are presented. A high-order discontinuous Galerkin spectral element method with finite-volume subcell shock capturing is employed to simulate the flow based on an implicit LES scheme and advanced over several buffeting cycles to reliably capture the shock unsteadiness. A study on the spanwise domain size shows that the shock oscillation amplitude decreases with increasing span, although its frequency and mean location remains fixed through the simulations. By comparing high- and low-resolution LES results, it is further presented that deviations from under-resolution are mostly limited to the separated region past the shock, where the high-fidelity results match experimental results more closely. In addition to the LES, low-fidelity URANS is shown to capture the shock unsteadiness correctly, but at a reduced amplitude and fails to match the force distributions on the blade surface. Through examination of instantaneous flow features, space-time relations and spectral proper orthogonal decomposition, a basic analysis of the shock-boundary layer interaction is presented and indicates that velocity perturbations travel upstream through the subsonic boundary layer and periodically cause oblique shock waves, transporting the information from the boundary layer into the passage.*

Keywords: large eddy simulation, discontinuous Galerkin, transonic flow, compressor cascade

Nomenclature

Roman letters

a = speed of sound [m s^{-1}]
c = chord length [m]
f = frequency [s^{-1}]
N = polynomial order
p = pressure [Pa]
$\mathbf{q}$ = vector of conserved variables
Q = Q-criterion [s^{-2}]
$\mathbf{R}$ = residual vector
s = surface arc length
$\mathbf{S}$ = strain rate tensor
t = pitch length [m]
t = time [s]
$\mathbf{u}$ = vector of Cartesian velocity components, $[u, v, w]^{\mathrm{T}}$
u, v, w = Cartesian velocity components [m s^{-1}]

Greek letters

α = finite-volume blending weight
β = inlet flow angle
ρ = density [kg m^{-3}]
ν = kinematic viscosity [m^2 s^{-1}]
ξ, η, ζ = streamwise, wall-normal, spanwise coordinates
$\mathbf{\Omega}$ = vorticity tensor

Dimensionless groups

C_f = skin friction coefficient
Re = Reynolds number, cU_{ref}/ν
Ma = Mach number, $\|\mathbf{u}\|_2/a$
St = Strouhal number, fc/U_{ref}

Superscripts and subscripts

avg = averaging interval
c = chord-based
DG = discontinuous Galerkin
FV = finite volume
in = inflow
is = isentropic
out = outflow
ref = reference
sep = separation
st = stagger angle
$+$ = wall units

1 Introduction

Jet engine compressors at transonic operating conditions are typically subject to strong unsteadiness caused by the oscillation of the shock structure. The transient behavior of the shock-boundary layer interaction (SBLI) results in unreliable performance of the engine [1,2] and cannot be properly captured by traditional Reynolds-averaged Navier-Stokes (RANS) codes used in the design process [3,4], hence leading to overly conservative design margins and compromised performance. To address the drawbacks of low-fidelity RANS, time- and space-resolved simulations such as Large Eddy Simulation (LES) and Direct Numerical Simulation (DNS) have seen a rise in popularity in the turbomachinery community over the last decade [5].

[1]Corresponding Author.
October 29, 2024

Given its complexity, the mechanisms driving SBLI remains a topic of current research [6]: The self-sustaining trailing-edge feedback mechanism proposed by Lee [7,8] has been observed in experimental [9], and numerical studies [10,11]. However other sources for unsteadiness have been suggested in the literature, such as the interaction with incoming turbulent structures [12] and the interaction of the shock with its self-induced separation bubble [13].

Given the many mechanisms that can cause the unsteadiness of the SBLI, an in-depth analysis of shock oscillations in transonic turbomachinery is of interest to mitigate such behavior in future designs. High-fidelity simulations, such as LES or DNS, of shock-buffeting phenomena on compressor blades have, however, remained scarce. This is, at least in part, due to the challenging nature of these flows as they require shock capturing methods, high spatial resolution to accurately model the typical high Reynolds numbers, and long run times to capture the typically low-frequency buffeting [13]. Bode et al. [14] recently analyzed the interaction of free-stream turbulence with the shock through highly resolved LES on a transonic compressor blade at realistic operating condition. High-fidelity compressor cascade simulations at different operating conditions were also conducted by Priebe et al. [15], who found evidence of the trailing edge feedback mechanism proposed by Lee [8]. Klose et al. [16] later evaluated a shock-capturing method for high-order Discontinuous Galerkin (DG) schemes on a transonic compressor cascade and analyzed a simple wall-modeled LES (WMLES) approach on the same setup [17].

Among the numerical methods used for these high-fidelity computations, high-order spectral methods have become a popular choice over the last few years [5], as they feature reduced dispersion and dissipation errors over lower-order schemes [18,19] and hence require fewer grid points for a given error margin. The discontinuous Galerkin spectral element method, in particular, has seen a number of recent developments that improve the numerical robustness and accuracy of the method [20–22] and has been proven to perform well in turbomachinery applications [23].

Building on the growing availability of computational resources and the demand for efficient, accurate and robust numerical schemes, the authors have recently published a series of papers [16,24,25] that introduces the high-order DG solver of *TRACE* from the German Aerospace Center (DLR) as vehicle towards a *Numerical Test Rig* based on LES. Across a number of different turbomachinery test cases, both subsonic and supersonic, the authors show good agreement with experimental results and have demonstrated the performance of the solver. This paper therefore aims to build up on the authors previous work by simulating complex phenomena in turbomachinery flows.

The current work is embedded in the DLR's holistic approach to study the SBLI phenomenon observed on the state-of-the-art Transonic Cascade TEAMAero (TCTA) through a combined research effort in the framework of the TEAMAero [26] consortium. In previous studies, three passages were measured simultaneously with High-Speed Schlieren (HSS) in order to reveal the interactions between adjacent passages showing a broad main frequency band of oscillation between 500 and 550 Hz, which is modulated by a strong high-frequency tone at 1140 Hz [27]. A further study on this cascade with High-Resolution Particle Image Velocimetry (PIV) and a Proper Orthogonal Decomposition (POD) analysis showed the different spatial modes of oscillation of the flow in the passage near the shock [28].

In the second part of this three-paper series aiming to identify the mechanisms of unsteady SBLI on the TCTA, we report results of high-fidelity simulations at the aerodynamic design point (ADP) condition. A high-order accurate Discontinuous Galerkin Spectral Element Method (DGSEM) with a finite volume (FV) subcell shock capturing approach tailored for the split-form DG method is used for the numerical discretization of the implicit LES scheme. Low-frequency shock oscillations are resolved through long simulation times, where time-resolved data sets are used to extract distinct features of the SBLI through flow field analysis and spatio-temporal correlations including results from Spectral Proper Orthogonal Decomposition (SPOD). The work includes a study of the spanwise domain size based on coarsely resolved LES, evaluation of the effect of spatial resolution and comparison to a low-order Unsteady Reynolds-Averaged Navier-Stokes (URANS) simulation. The simulations are compared and validated against experimental results presented in the first part of this paper series and provide validity for the in-depth SBLI analysis presented in the third part. The combination of experimental studies and high-fidelity LES capturing low-frequency buffeting through long simulation times offers a unique perspective on the SBLI mechanism found in transonic compressor applications.

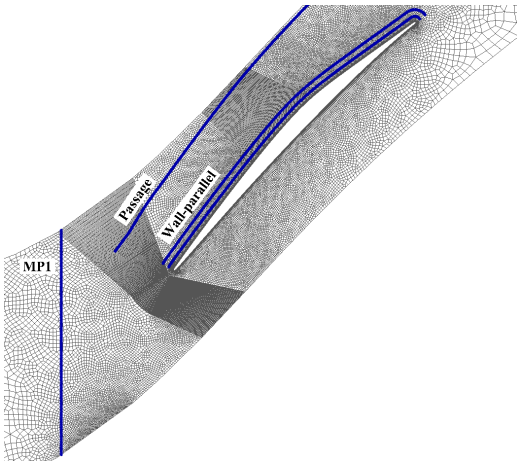

Fig. 1 Computational grid (coarse) around the blade together with selected probe locations. Only elements without interior Legendre-Gauss-Lobatto (LGL) nodes shown.

2 Numerical method

All numerical results presented in this paper are based on DLR's compressible flow solver for turbomachinery applications *TRACE*. A FV method is used for the discretization of the URANS equations [29,30] in combination with the Menter SST k-ω model [31] for the modeling of turbulence, where the production term is modified according to Kato and Launder [32]. The two-equation γ-Re_θ model by Langtry and Menter [33] accounts for laminar-to-turbulent transition. A 2^{nd} order scheme is employed based on the Green-Gauss gradient method and the limiter by Venkatakrishnan [34] in combination with Roe's approximate Riemann solver [35].

The LES is performed with the high-order DG solver of *TRACE* [36]. The implementations have been extensively described and tested [16,24,25,36,37] and only a brief overview is given here. A nodal collocation approach is used for the DGSEM, where the interpolation and quadrature points are both taken to be the LGL nodes and yield an efficient numerical scheme with diagonal mass matrix [38]. The implicit (no-model) LES approach is chosen for the modelling of subgrid stresses, such that dissipation is added implicitly via the numerical dissipation of the Riemann solver. Numerical errors arising from the non-linearity of the advective fluxes and the limited precision of integration are addressed by employing kinetic-energy or entropy conserving split-form approximations of the inviscid fluxes [21,22], which cancel numerical errors and stabilize the high-order scheme. In this work, we apply the entropy-conserving split-form variant by Chandrashekar [39] together with the corresponding Riemann solver. The Bassy-Rebay-1 (BR1) scheme [40] is applied for discretization of the viscous part with a central numerical flux at the element interfaces.

To reduce spurious oscillations across shock fronts in the high-order accurate LES, the FV subcell shock capturing method by Hennemann et al. [41] is applied in elements subject to shock

Table 1 Overview of simulation parameters for the TCTA compressor cascade

Case	Ma_{in}	Re_{in} $/10^6$	β_{in}	L_z/c	N	nDoF $/10^6$	nMPI	CPUh $/t_c$	$\overline{\Delta\xi^+}$	$\overline{\Delta\eta^+}$	$\overline{\Delta\zeta^+}$	$\Delta t/t_c$ $\times 10^6$	t_{avg}/t_c
LES5	1.20	1.34	145.6°	0.05	3	54.6	4 096	15 583	41.2	2.03	31.4	11.2	60.0
LES10	1.21	1.35	145.8°	0.1	3	109.0	8 192	30 933	40.3	1.99	30.7	11.2	40.0
LES20	1.22	1.34	145.5°	0.2	3	218.0	16 384	77 950	39.7	1.96	30.2	11.2	40.0
LES10-HR	1.21	1.34	145.7°	0.1	3	375.2	16 384	152 850	25.5	1.39	21.4	7.5	75.0
URANS	1.21	1.34	145.6°	-	-	0.12	1 024	74.6	-	<1	-	27.9	50

nDoF = number of degrees of freedom; nMPI = number of MPI ranks; $t_c = c/U_{in}$; $\overline{\square^+} = \frac{1}{s}\int_0^s \square^+(\hat{s})\mathrm{d}\hat{s}$.

waves and locally blends the high-order operator with a first-order FV scheme:

$$\frac{\partial \mathbf{q}}{\partial t} + \alpha \mathbf{R}^{\mathrm{FV}}(\mathbf{q}) + (1-\alpha)\mathbf{R}^{\mathrm{DG}}(\mathbf{q}) = 0. \tag{1}$$

Here, $\mathbf{R}$ is the inviscid residual operator, $\mathbf{q}$ is the vector of conserved variables and $\alpha \in [0,1]$ is the blending factor based on a shock indicator function. In accordance with the results by Klose et al. [16], we employ the feature-based dilatation-vorticity sensor by Fernandez et al. [42] for the identification of the troubled elements. The time and space relaxation factors of the sensor are both set to 0.7, in accordance with [43].

Both, DGSEM-LES and FV-URANS are advanced in time with an explicit third-order Runge-Kutta scheme [44].

3 Setup

We simulate the flow over the TCTA cascade at ADP operating condition with $\mathrm{Ma}_{in} = 1.21$, $\mathrm{Re}_{in} = 1.35\times10^6$ and $\beta_{in} = 145.7°$, where the subscript 'in' refers to measurement plane 1 (MP1) located half a pitch upstream of the leading edge. The pitch is $t = 0.065$m, the chord length $c = 0.1$m and the stagger angle $\beta_{st} = 135.8°$. All quantities presented in this paper are non-dimensionalized by means of reference quantities recorded at the MP1, with the convective time being defined as $t_c = c/U_{ref} = c/\|\mathbf{u}_{in}\|_2$, which is approximately 2.7×10^{-4}s for all simulations. We refer to the first part of this paper series, as well as to Munoz Lopez et al. [45], for a more detailed description of the experimental compressor cascade setup.

The mesh is constructed such that the inlet boundary is located one chord length upstream of the leading edge and the outlet panel is 1.5 chord lengths downstream from the trailing edge. The inflow and outflow boundary conditions in all simulations are the one-dimensional non-reflecting boundary conditions following Schlüß et al. [46], with the total pressure, total temperature and flow angle specified at the inflow plane and static pressure at the outflow plane. Periodic boundary conditions are set along the spanwise and pitchwise domain faces. No inflow turbulence is prescribed at the inlet, given that experimental values are below 1% and the effects are assumed to be minor at most.

Different computational grids generated with the Gmsh package [47] are employed in this study: a coarser grid with 47 319 elements in the x-y plane is used for a domain size study, while a refined grid with 108 564 elements per plane is used for the final LES. A polynomial order of $N = 3$ is used in all LES, yielding a 4^{th} order accurate spatial discretization. For the domain study of the LES, the coarse grid is extruded by 5%, 10% and 20% chord length, whereas the fine grid is extruded by 10% chord length. All grids are constructed with a structured refinement around the shock location to limit spurious waves and resolve the steep gradient adequately. The METIS library [48] is used for the domain decomposition into local blocks required for Message Passing Interface (MPI) parallelization. A plot of the coarse computational grid around the blade (without the interior LGL nodes) is given in Fig. 1, together with the locations of the most relevant probes used in this paper.

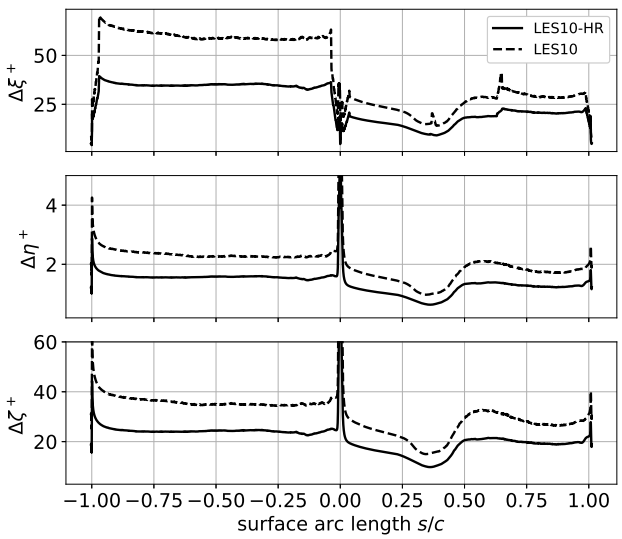

Fig. 2 Non-dimensional cell sizes of the low- and high-resolution LES normalized by the polynomial order

Preliminary URANS studies are used to iterate the operating condition in order to closely match the values in the experimental campaign (see the first part of this paper series). Because the setup has no geometric variation along the span, a single spanwise element is used for the URANS studies. The solution is then interpolated onto the coarse LES grid, and, after several through flows, interpolated onto the fine mesh.

The mean non-dimensional cell-spacings for the coarse and fine mesh are given in Fig. 2 for the streamwise (ξ), wall-normal (η) and spanwise (ζ) coordinates. Negative s/c correspond to the pressure side while positive values represent the suction side. The cell-spacings are normalized by the polynomial order N to aid the comparability to FV simulations. Excluding the leading and trailing edge, the maximum non-dimensional cell sizes for the coarser grid are $\Delta\xi^+_{max} = 65$, $\Delta\eta^+_{max} = 2.5$ and $\Delta\zeta^+_{max} = 40$, and for the refined grid $\Delta\xi^+_{max} = 35$, $\Delta\eta^+_{max} = 2$ and $\Delta\zeta^+_{max} = 25$. The values are comparable to other high-Reynolds number compressor studies [14,16] and the resolution is deemed sufficient for LES. A summary of the simulation parameters is given in Tab. 1.

For the remainder of the paper, the coordinate system will be rotated such that the x-axis aligns with the inflow direction to be consistent with experiments. All surface quantities are evaluated in a coordinate system aligned with chord of the blade.

4 Flow field

A plot of instantaneous three-dimensional structures present in the LES10-HR case is given in Fig. 3: vortical structures are extracted through an iso-surface of $Q \equiv (\|\mathbf{\Omega}\|^2 - \|\mathbf{S}\|^2)/2$, shocks and shocklets are highlighted through an iso-surface of Ma = 1 and contours of numerical schlieren ($\|\nabla\rho\|$) are plotted in the back-

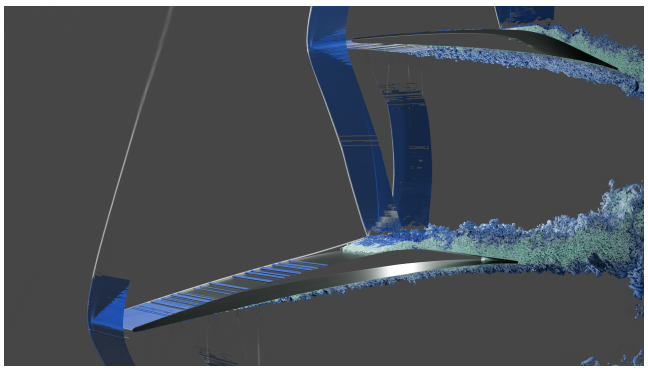

Fig. 3 Vortical structures highlighted by iso-surface of Q

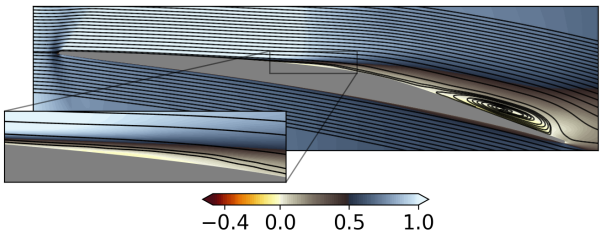

Fig. 4 Time-averaged streamlines and contours of $\overline{u}/\|\mathbf{u}_{in}\|_2$ for LES10-HR

ground. The flow is characterized by a laminar boundary layer on the suction side up to the bow shock at mid-chord, which extends down from the upper blade's leading edge. Planar waves, called shocklets, travel upstream within the passage and intermittently transition the laminar boundary layer on the blade's pressure side as they impose an adverse pressure gradient on the flow.

Time-averaged streamlines plotted over contours of the inflow-aligned velocity component $\overline{u}/\|\mathbf{u}_{in}\|_2$ in Fig. 4 shows that the averaged flow field is characterized by slender separation bubble underneath the shock wave (shown by the detail plot) and a trailing large recirculation zone that expands until the trailing edge, indicating an open separation bubble.

5 Domain Study

We start the discussion by evaluating the impact of the resolved spanwise domain size L_z. The length must to be chosen large enough to have as little impact on the results as possible under the limitation of the available computational resources. The goal of this study is, however, not to establish when the solution will be fully converged, but rather assess the deviation with respect to an acceptable margin such that the shock oscillation mechanism is no longer significantly affected.

We simulate the flow through the TCTA on the coarser grid with three different spanwise domain size: 5% (LES5), 10% (LES10) and 20% (LES20) chord length. The impact of L_z is evaluated by comparison of the time-averaged isentropic Mach number Ma_{is} (Fig. 5(*a*)), the skin friction coefficient C_f (Fig. 5(*b*)) and the frequency spectrum of the shock oscillation recorded along the mid-passage probe (Fig. 5(*c*)). Time-averaged streamlines are given in Fig. 6 (but for smaller averaging windows of 30–40 convective time units). In the plots of the surface quantities, error bars indicate the 90% confidence interval of the temporal fluctuations computed with the method described by Bergmann et al. [49].

Notably in Fig. 5(*a*), the LES5 case shows a lower Ma_{is} value upstream of the shock ($0 > x_c/c\ 0.4$) on the suction side and a higher value past the shock ($x_c/c\ > 0.5$) than both LES10 and LES20. The LES5 case also shows a larger region of separated flow at the trailing edge, as indicated by a drop in C_f, and an increase in Ma_{is} starting at $x_c/c > 0.6$. As a result, the overall pressure distribution is modified, as the blockage within the cascade is increased by the larger flow displacement. Differences between LES10 and LES20 are limited to the separation and reattachment points (roots of C_f) and the transition point (peak in negative C_f) of the upstream separation bubble (see Fig. 4): The LES20 separates earlier and its peak downstream of the reattachment point is reduced. The simulations converge again for $x_c/c > 0.7$. On the pressure side, LES10 and LES20 are closely aligned until $x_c/c > 0.7$, while the LES5 case deviates considerably along the midsection of the blade. We note, however, that the deviations are within the confidence intervals indicated by the error bars and even longer simulation times are needed to further converge the results. The observations made above are confirmed by the changes in separation bubble shape in Fig. 6, which decreases in size as L_z increases. But just as the surface plots, we note that the time-averaged streamlines are still subject to statistical uncertainty.

The shock oscillation is evaluated along the mid-passage probe (see Fig. 1) and Welch's power spectral density (PSD) estimate of $x_c/c|_{\mathrm{Ma}=1}$ is plotted in Fig. 5(*c*) for all three domain sizes. The results are also summarized in Tab. 2, where the non-dimensional frequency peak ft_c (also termed Strouhal number, St) is given together with the mean shock location $\overline{x_s/c}$, the maximum oscillation amplitude $\Delta_{\max}(x_s/c)$, and its standard deviation $\mathrm{std}(x_s/c)$. The buffeting shows the same distinct peak for all cases and the mean shock location is also closely aligned. Differences arise in the higher frequencies, where the LES5 case has a number of peaks not visible in the other cases. The oscillation amplitude is also much increased in the LES5 case (0.28) over the LES10 (0.17) and LES20 (0.16) cases.

Overall, the results show that while the deviations are related to the separation bubble mechanics past the shock, its oscillation frequency is (almost) not affected by the spanwise domain size, although the amplitude of the shock movement decreases significantly between LES5 and LES10. This observation partially agrees with the findings by Touber and Sandham [13] in their study of SBLI under an oblique shock wave, as they also found a strong sensitivity of the separation bubble size with respect to the length of the span, with taller bubbles existing on narrower domains. However, it was suggested that the increased levels of reverse flow in taller bubbles directly affect the shock oscillations, and a good agreement with experimental results could only be achieved by basing the Strouhal number on the separation length L_{sep} with $\mathrm{St}_{\mathrm{sep}} = fL_{\mathrm{sep}}/U_{\mathrm{ref}} \approx 0.03$. The shock oscillation frequency in the present work, however, appears to be less dependent on the bubble size. Nevertheless, with the above definition of $\mathrm{St}_{\mathrm{sep}} \approx 0.03$, a separation length of $L_{\mathrm{sep}}/c \approx 0.18$ can be determined for the frequencies recorded. This value matches the observed separation lengths at mid-chord in Fig. 5(*b*) well ($0.12 \leq L_{\mathrm{sep}}/c \leq 0.22$).

6 Resolution assessment and URANS comparison

In this section, we compare the high-resolution LES (LES10-HR) with the LES10 case, URANS and experimental results (see first part of this paper series). For the high-resolution LES, a span of 10% was chosen as a compromise between domain size and number of convective times simulated, given that the computational cost scales linearly for both. The boundary conditions for LES10-HR are kept consistent with the lower resolution cases. The operating condition determined by the Mach number, Reynolds number and flow angle is summarized in Tab. 1 and shows good agreement with experimental data ($\mathrm{Ma}_{in} = 1.21$, $\mathrm{Re}_{in} = 1.35{\times}10^6$ and $\beta_{in} = 145.7°$). The corresponding isentropic Mach number and skin friction coefficients are given in Fig. 7(*a*) and Fig. 7(*b*), together with results from URANS and the experimental campaign. The spectrum of the shock oscillation recorded along the mid-passage probe are plotted in Fig. 7(*c*).

All isentropic Mach numbers obtained from the simulations are in agreement upstream of the shock (x_c/c <,0.3), where they are consistently slightly above the experimental values, although the

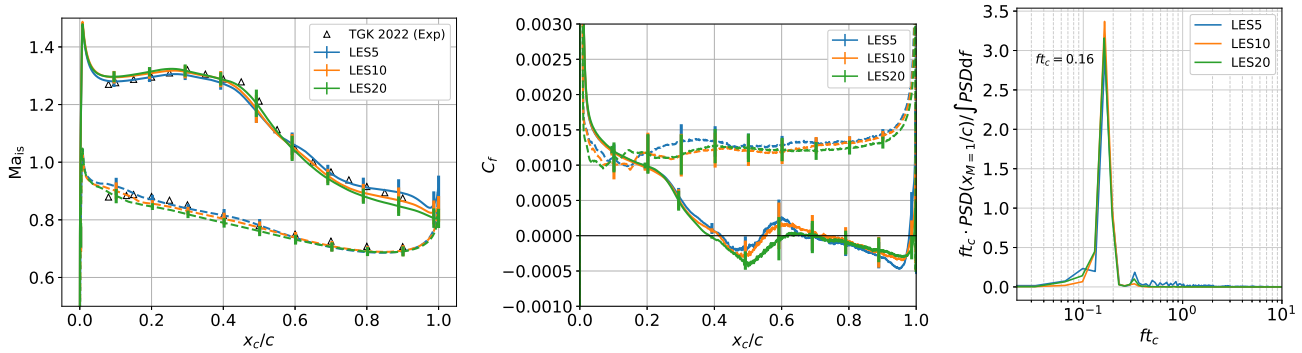

(*a*) Isentropic Mach number (*b*) Skin friction coefficient (*c*) Shock oscillation spectrum

Fig. 5 Comparison of isentropic Mach number, skin friction coefficients and shock oscillations spectrum for different spanwise domain sizes and experiments. Solid lines indicate the suction side, dashed lines the pressure side.

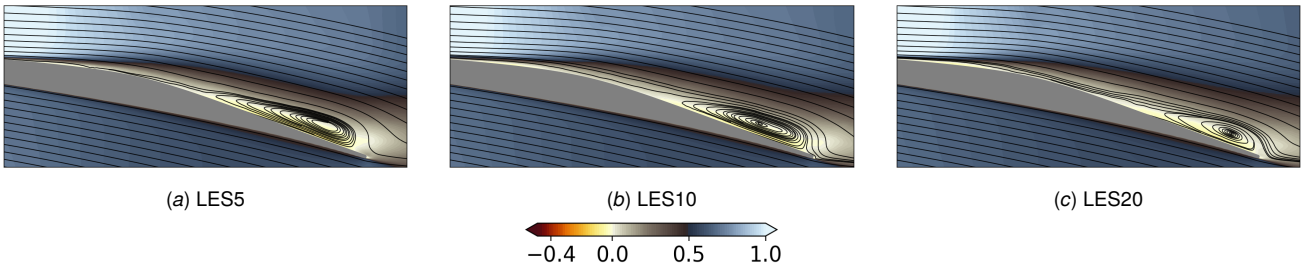

(*a*) LES5 (*b*) LES10 (*c*) LES20

Fig. 6 Time-averaged streamlines and contours of $\overline{u}/\|\mathbf{u}_{\mathbf{in}}\|_2$

error bars infringe on the experimental markers. Differences between the LES10-HR and the LES10 case are minor and limited to the separated flow region downstream of the shock ($x_c/c > 0.6$). Here, the high-resolution shows slightly higher values and matches the experiments better. At $x_c/c > 0.3$, the URANS starts to deviate from the LES results and does not predict the plateau in the region $0.3 < x_c/c < 0.4$ and an earlier shock location results in a mismatch of the curves for $x_c/c > 0.4$.

An explanation is given in Fig. 7(*b*): both LES show an earlier drop in C_f on the suction side upstream of the shock location (at $x_c/c \approx 0.2$), which is driven by an intermittent thickening of the boundary layer resulting in an oblique shock wave (see Section 7.1). The suction side flow in the URANS remains unperturbed until $x_c/c = 0.3$ and does not exhibit any larger oscillations, as indicated by the negligible height of the error bars (indicating the periodic oscillations present in the URANS) until the separated region ($x_c/c > 0.6$). The URANS also under-predicts the isentropic Mach number on the pressure side until $x_c/c \approx 0.6$, while both LES10-HR and LES10 match the experiments closely. Here, the skin friction of the URANS drops to substantially lower values than any LES, which indicates that the flow is predicted to be mainly laminar, while the flow in the LES is driven by intermittent turbulence (see Section 7.1). This results in higher values of C_f and larger oscillation amplitudes (as seen by the error bars).

Figure 7(*c*) shows the spectrum of the shock oscillation recorded along the mid-passage probe for the LES10-HR, LES10 and URANS cases and the data are summarized in Tab. 2. Remarkably, all simulations report the same Strouhal number of $St \approx 0.16$, which slightly overestimates the experimental values of approximately 0.14. We note, however, that the URANS require a small time-step size of $\Delta t/t_c = 2.8\times10^{-5}$ because the shock oscillation magnitude and frequency are otherwise not correctly predicted.

As noted before, the mean shock location in the URANS is upstream compared to the LES and the oscillation amplitude is less than half compared to the LES20 case. Given that the LES10-HR also reports a larger oscillation amplitude (0.23) compared to the LES10 case (0.17), we assume that the increased numerical dissipation of the URANS and, to a lesser extent, the coarser LES, damps out flow structures that are driving the larger shock oscillations in the LES10-HR. We note, however, that the cell sizes used for the LES10-HR are typical for LES studies (e.g. [14]) and that the solution obtained from the coarser grids should be considered under-resolved. In the experiments, a shock oscillation amplitude of $\Delta_{\max}(x_s/c) = 0.13$ is reported, which agrees very well with the LES20 case, although a high-resolution study that case would presumably show larger deviations as well. A possible explanation for the differences in the buffeting quantities between simulations and experiments is the much larger (but finite) spanwise domain size used in the wind tunnel ($L_{z,\mathrm{TGK}} = 1.68c$), that might allow for some spanwise modulation of the shock.

Table 2 Shock oscillation quantities

Case	ft_c	$\overline{x_s/c}$	$\Delta_{\max}(x_s/c)$	$\mathrm{std}(x_s/c)$
LES5	0.165	0.537	0.278	0.065
LES10	0.164	0.531	0.172	0.054
LES20	0.163	0.528	0.158	0.046
LES10-HR	0.163	0.535	0.231	0.058
URANS	0.161	0.504	0.072	0.024

7 Shock-boundary layer interaction

In the following paragraphs, we discuss the shock-boundary layer interaction and the resulting flow topology and space-time correlations. We present results from both, the LES20 and the LES10-HR cases, as these most closely match the experimental data.

7.1 Shock oscillation. The sequence of the shock oscillation is presented in Fig. 8 and Fig. 9, where one period (i.e. approx-

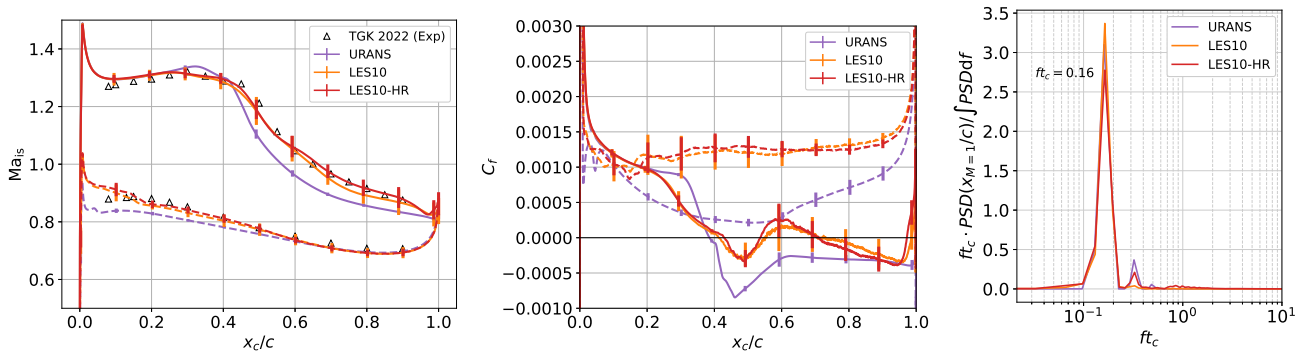

(*a*) Isentropic Mach number (*b*) Skin friction coefficient (*c*) Shock oscillation spectrum

Fig. 7 Comparison of isentropic Mach number, skin friction coefficients and shock oscillations spectrum from the LES10, LES10-HR, URANS and experiments. Solid lines indicate the suction side, dashed lines the pressure side.

imately 6.3 t_c) is given through nine snapshots along the center plane for both LES10-HR and LES20. The sequence starts with the shock at its most forward position (a). The strong adverse pressure gradient underneath the normal shock forces the boundary layer to separate and reattach. Upstream traveling disturbances within the subsonic boundary layer cause it to thicken and result in an intermittent oblique compression wave (b) (see also Section 7.3). Because the flow angle changes instantly across oblique shock waves, it forces the boundary layer to lift off further to align with the higher flow incidence. As the shock moves downstream towards the maximum thickness of the blade (c–e), the adverse pressure gradient further increases through the downward curving of the blade and the separated flow fails to reattach. Shocklets travel upstream within the passage as planar waves (a–c), combine (d–e) and lift off the boundary layer on the pressure side, causing the flow to transition (e–f).

While the shock remains in the most downstream position (e–g), the separated fluid region continues to grow and forces the flow above to become locally supersonic again as the passage cross section is narrowed by the added displacement thickness of the boundary layer. Because information can travel upstream within the subsonic boundary layer, the separation point continues to move upstream (e–f) and causes the emergence of an oblique compression wave. The compression wave lowers the Mach number downstream and, as the shocklets merge with the main shock (f–g), it is pushed upstream and off the leading edge. As the boundary layer is given space to reattach, the recirculating fluid is shed off the blade and forms a large-scale vortex (h–i) while the shock has returned to its initial position and the process starts over. For a more detailed description of the underlying mechanism, we refer to the third part of this paper series.

Comparison of Fig. 8 and Fig. 9 shows that the underlying SBLI mechanics are identical for the two LES. The main difference is rooted in the larger region of separated flow in the LES10-HR (g–h), which in turn causes an increased Mach number above. Pressure waves and shocklets in the LES20 simulation also appear more diffused, given the increased numerical dissipation in this case. For the remainder of the result sections, only the LES10-HR case considered.

7.2 Spatio-temporal analysis. The space-time diagrams of the pressure in Fig. 10 further support the previously introduced SBLI mechanics: within the subsonic region ($x_c/c > 0.6$), pressure waves can travel in both directions and thin streaks of high pressure with negative slope represent the shocklets observed in Fig. 8 and Fig. 9. Within the supersonic flow region ($0.1 < x_c/c < 0.5$), pressure information only travels downstream and all streaks have a positive inclination, except for a series of thin lines of higher pressure that represent the oblique compression waves. As the boundary layer lifts off, the compression waves also move upstream and thereby link the boundary layer with the passage flow. The diagram further highlights that the oblique compression waves appear to be driven by the shocklets: because they impose an additional adverse pressure force on the boundary layer and cause it to lift off further, resulting in upstream traveling disturbances and a compression wave.

Close to the wall ($\eta = 0.003c$, Fig. 11), the sonic line no longer follows the regular sinusoidal pattern that governs the motion at mid-passage, but is dominated by a high-frequency oscillation. Here, the sonic line is driven by the boundary layer dynamics and the oblique shock waves.

A summary of the different shock oscillation frequencies that occur in the domain is given by the spectra in Fig. 12. Here, the mid-passage probe is plotted together with four wall-normal probes at different displacements heights in the range $0.003c \leq 0.035c$. Secondary peaks occur at multiples of the principal buffeting frequency, i.e. $ft_c = 0.32$ and $ft_c = 0.48$, which is consistent with the observation of the oblique compression wave (Fig. 8). Further evaluation of the frequencies and their spatial correlation is given in the following section.

7.3 SPOD. In order to capture the dominant flow field features at the detected shock oscillation frequencies, we conduct a SPOD analysis of the center slice. The SPOD is computed with an implementation of the algorithm published by Schmidt and Colonius [50] and recently applied by Morsbach et al. [51], where we assemble a matrix of M snapshots $\mathbf{X} \in \mathbb{C}^{M \times N}$, decompose the matrix along its time axis into N_{blk} overlapping blocks (Welch's spectral estimation method) and apply a discrete Fourier transform on each block after multiplication of the data by a Hamming window. The result is a set of N_{blk} Fourier transformed blocks $\widetilde{\mathbf{X}}_k$ with N_{fft} frequencies each:

$$\widetilde{\mathbf{X}} = \begin{pmatrix} — & \widetilde{\mathbf{x}}_1^H & — \\ & \vdots & \\ — & \widetilde{\mathbf{x}}_{N_{\text{blk}}}^H & — \end{pmatrix} \in \mathbb{C}^{N_{\text{blk}} \times N}, \tag{2}$$

where N is the number of spatial points times the number of variables. At each frequency, the covariance matrix

$$\widetilde{\mathbf{C}} = \frac{1}{N_{\text{blk}}} \widetilde{\mathbf{X}}^H \widetilde{\mathbf{X}} \in \mathbb{C}^{N \times N}, \tag{3}$$

is computed and the SPOD modes are obtained by solving the eigenvalue decomposition of the covariance matrix [50]:

$$\widetilde{\mathbf{C}}\mathbf{W}\mathbf{\Phi} = \mathbf{\Lambda}\mathbf{\Phi}, \quad \mathbf{W} = \text{diag}\,(w_1, \ldots, w_N)\,. \tag{4}$$

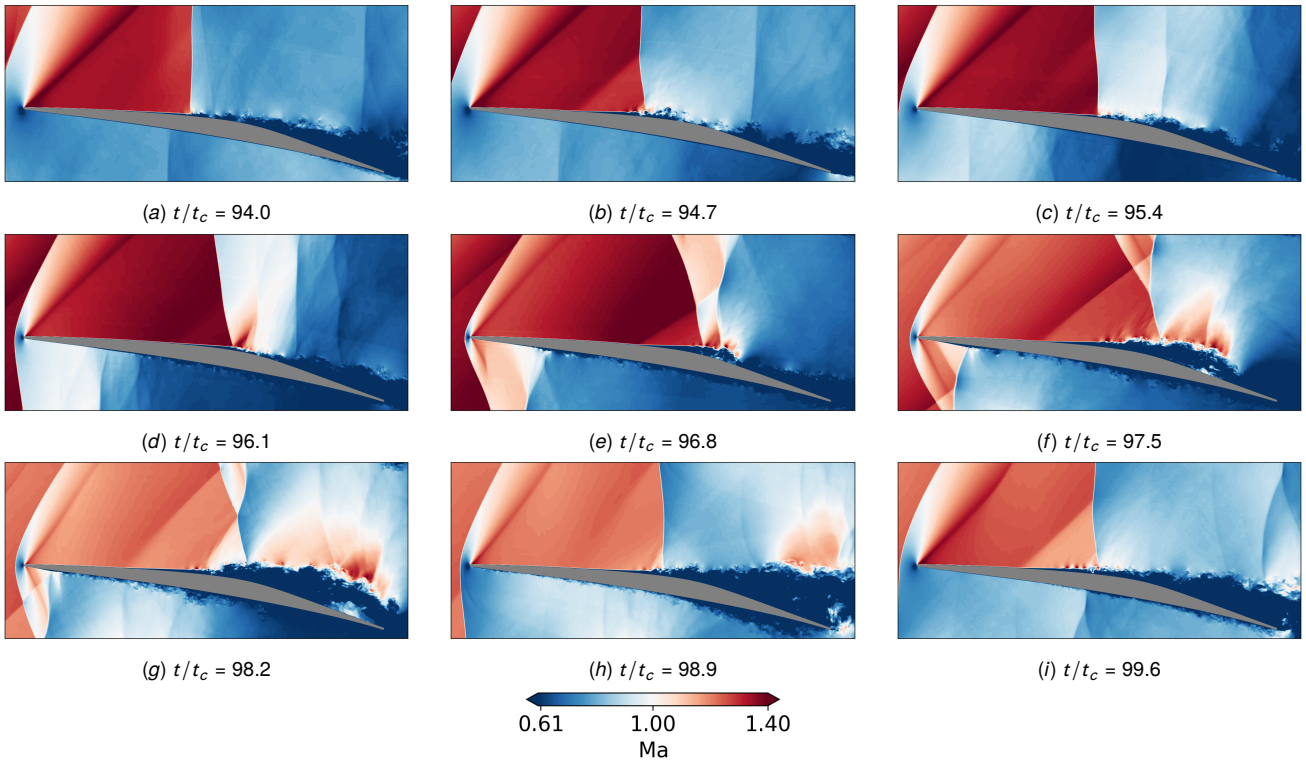

Fig. 8 LES10-HR: Time series of Mach number contours over one shock oscillation period.

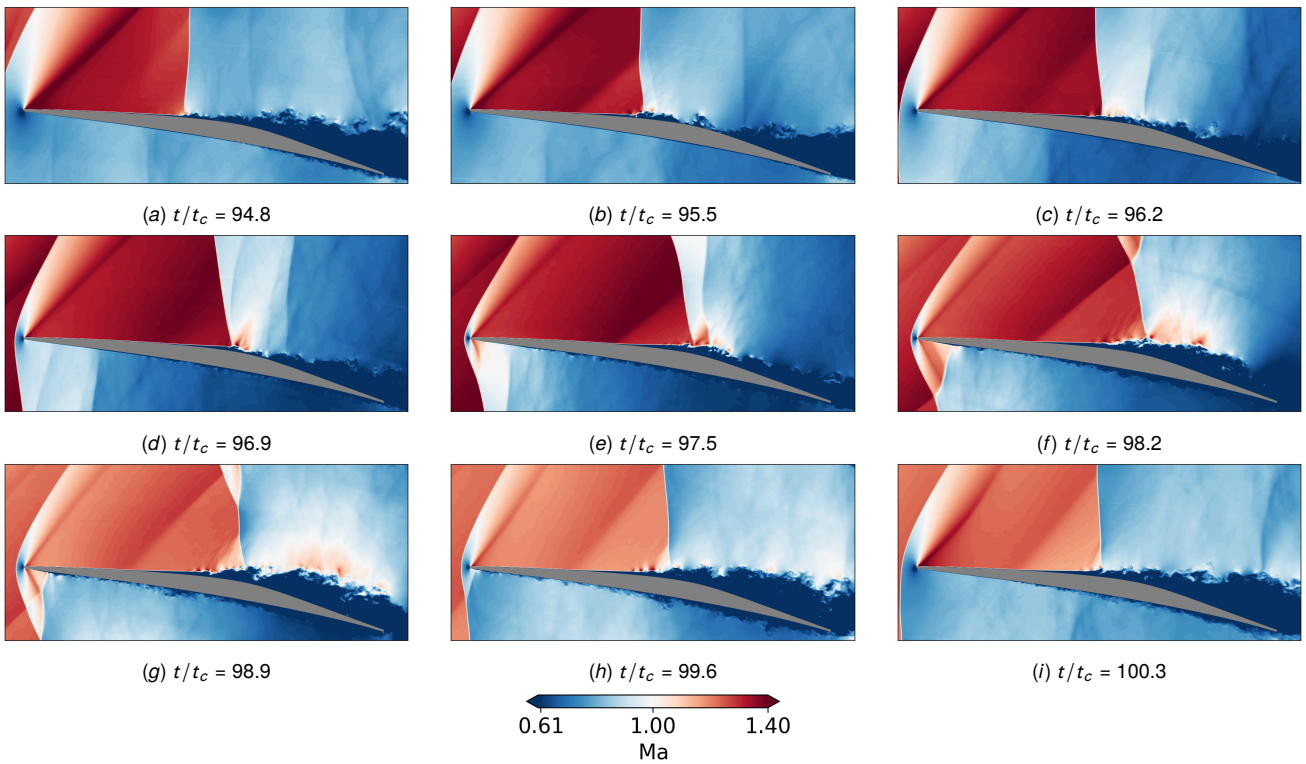

Fig. 9 LES20: Time series of Mach number contours over one shock oscillation period.

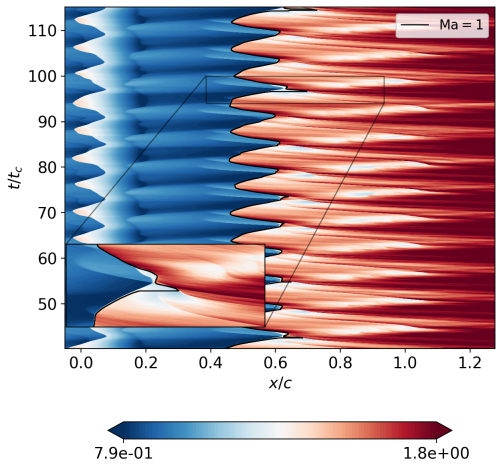

Fig. 10 Space-time diagram of the pressure p/p_{in} along the mid-passage probe.

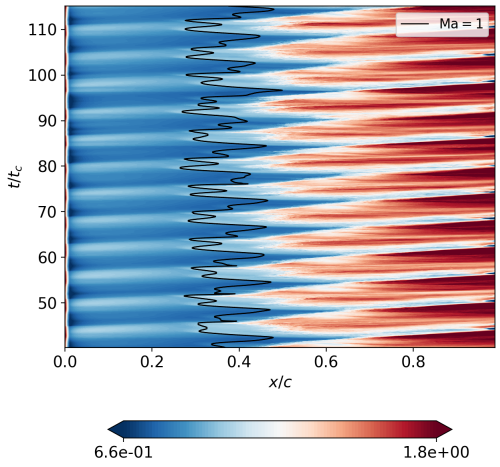

Fig. 11 Space-time diagram of the pressure p/p_{in} along the suction side of the wall-normal probe displaced by η = 0.003c.

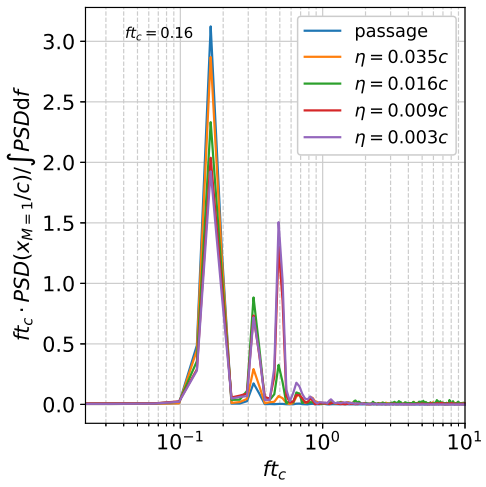

Fig. 12 Spectra of the shock oscillation for the mid-passage probe and various wall-normal probes with different distances η.

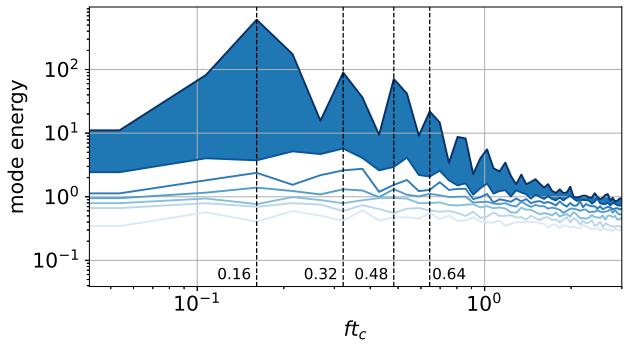

Fig. 13 SPOD eigenvalues

In the equation above, $\mathbf{W}$ is a weight matrix, $\mathbf{\Phi}$ are the eigenvectors and $\mathbf{\Lambda}$ the eigenvalues.

To be consistent with the experiments, we calculate the SPOD based on the turbulent kinetic energy (TKE) norm with uniform weights and the velocity components as the input vector:

$$\mathbf{X} = \left[u',\ v',\ w'\right]^{\mathrm{T}},$$
$$\mathbf{W} = \int_V \mathrm{diag}\,(1,\ 1,\ 1)\,\mathrm{d}V. \tag{5}$$

A total of 1008 snapshots over 75 convective times is used and decomposed into 7 blocks with a size of 250 snapshots each and 50% overlap. The evaluation window is selected to be in accordance with the analysis region used in the experimental campaign in the first part of this paper series. The mode energy sorted by frequencies is given in Fig. 13 and shows a distinct dominant peak with significant separation between the first and the second mode at the main buffeting frequency of $0.16/t_c$. The next peaks occur at the second ($ft_c = 0.32$), third ($ft_c = 0.48$), and fourth harmonic ($ft_c = 0.64$), at which frequencies the shock-oscillation in the near-wall region also spike (see Fig. 12).

The mode shape at $ft_c = 0.16$ distinctly shows the streamwise back-and-forth motion of the normal shock at mid-blade in the u velocity component (indicated by arrows). Underneath the shock, the sign of the mode reverses, which is attributed to fluctuations in the opposite flow direction due to the strong oblique waves occurring at this frequency. This process is outlined in Fig. 8(d–f), where the downstream movement of the normal shock is accompanied by an upstream movement of the the oblique shock and the associated upstream thickening of the boundary layer. Downstream movement of the shock is therefore accompanied by increased reversed (u') and vertical (v') flow. A thin line in u' motion also extends further upstream than the mean shock location which is attributed to disturbance in the upstream direction within the boundary layer when the separation bubble moves. The oblique compression wave, however, is more distinctly represented by the higher frequency modes at $ft_c = 0.48$ and $ft_c = 0.64$, which highlight vertical displacement of the fluid (v') in the shape of the oblique compression wave (indicated by arrows). This observation is consistent with the snapshot series in Fig. 8, where the oblique compression waves occurs multiple time over one buffet cycle.

The dominant SBLI motion can hence be summarized as follows: as the shock wave moves towards its most downstream location, the separation bubble grows substantially and forces velocity perturbations upstream through the subsonic boundary layer. Fluctuations of the bubble occur at higher frequencies with upstream traveling shocklets interacting with the separation bubble

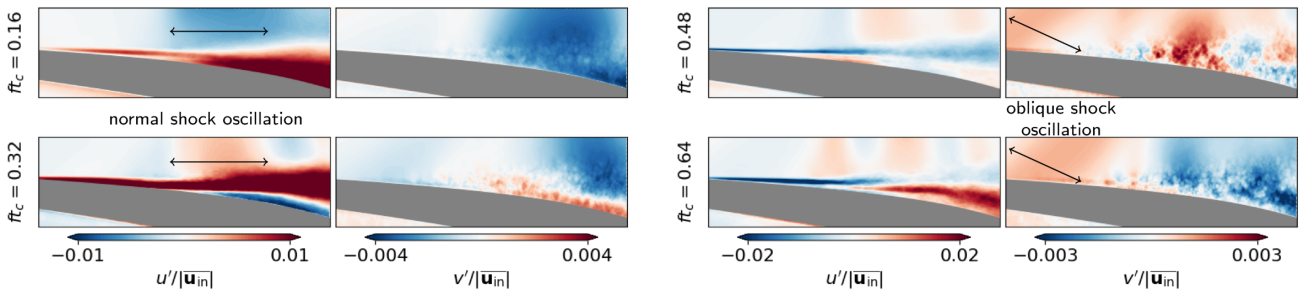

Fig. 14 First SPOD modes for the dominant frequencies

and causing the emergence of oblique compression waves. For a more in-depth discussion of the SBLI mechanism, we refer to the third part of this paper series.

8 Conclusion

In the second part of this three-paper series, we have focused on the high-fidelity LES of the TCTA at the transonic ADP with $\mathrm{Re}_{in} = 1.35\times10^6$ and $\mathrm{Ma}_{in} = 1.21$. The implicit LES scheme employed is based on a high-order discontinuous Galerkin spectral element method with a FV subcell shock capturing scheme. Overall, a very good match with the experimental campaign (first part of this paper series) is achieved, with a near exact match of the isentropic Mach number and a close agreement of the shock oscillation frequency ($\mathrm{St}_{LES} = 0.16$, $\mathrm{St}_{exp} = 0.14$). A study with spanwise domain sizes 5%, 10% and 20% chord length showed that the smaller domain sizes overestimate the transition and reattachment peaks, pointing to their larger separation bubbles. Further, the shock oscillation amplitude decreases with increasing span, although its frequency remains fixed through the simulations. Differences between high- and low-resolution LES are shown to be less significant and are mostly limited to the separated region past the shock, where the high-fidelity results match experimental results slightly better. We also perform a basic analysis of the SBLI and show that velocity perturbations travel upstream through the subsonic boundary layer and periodically cause oblique shock waves, which transport the information from the boundary layer into the passage.

As part of our future effort, we plan to report on the effect of resolving multiple passages and to evaluate and improve practices for low-fidelity URANS simulations.

Acknowledgments

The simulations were performed on the national supercomputer HPE Apollo Hawk at the High Performance Computing Center Stuttgart (HLRS) under the grant number TCTA-SBLI/44238.

References

[1] Epstein, A. H., Kerrebrock, J. L., and Thompkins, W. T., 1979, "Shock Structure in Transonic Compressor Rotors," AIAA Journal, **17**(4), pp. 375–379.

[2] Hah, C. and Reid, L., 1992, "A Viscous Flow Study of Shock-Boundary Layer Interaction, Radial Transport, and Wake Development in a Transonic Compressor," Journal of Turbomachinery, **114**(3), pp. 538–547.

[3] Vieira, R. and Azevedo, J. L., 2013, "RANS Simulations of Flows with Shock Wave-Boundary Layer Interaction," *51st AIAA Aerospace Sciences Meeting including the New Horizons Forum and Aerospace Exposition*, American Institute of Aeronautics and Astronautics, doi: 10.2514/6.2013-985.

[4] Hergt, A., Klinner, J., Wellner, J., Willert, C., Grund, S., Steinert, W., and Beversdorff, M., 2019, "The Present Challenge of Transonic Compressor Blade Design," Journal of Turbomachinery, **141**(9).

[5] Sandberg, R. D. and Michelassi, V., 2019, "The Current State of High-Fidelity Simulations for Main Gas Path Turbomachinery Components and Their Industrial Impact," Flow, Turbulence and Combustion, **102**(4), pp. 797–848.

[6] Clemens, N. T. and Narayanaswamy, V., 2014, "Low-Frequency Unsteadiness of Shock Wave/Turbulent Boundary Layer Interactions," Annual Review of Fluid Mechanics, **46**(1), pp. 469–492.

[7] Lee, B. H. K., 1990, "Oscillatory shock motion caused by transonic shock boundary-layer interaction," AIAA Journal, **28**(5), pp. 942–944.

[8] Lee, B., 2001, "Self-sustained shock oscillations on airfoils at transonic speeds," Progress in Aerospace Sciences, **37**(2), pp. 147–196.

[9] Hartmann, A., Feldhusen, A., and Schröder, W., 2013, "On the interaction of shock waves and sound waves in transonic buffet flow," Physics of Fluids, **25**(2), p. 026101.

[10] Crouch, J. D., Garbaruk, A., Magidov, D., and Travin, A., 2009, "Origin of transonic buffet on aerofoils," Journal of Fluid Mechanics, **628**, pp. 357–369.

[11] Garnier, E. and Deck, S., 2010, "Large-Eddy Simulation of Transonic Buffet over a Supercritical Airfoil," *Notes on Numerical Fluid Mechanics and Multidisciplinary Design*, Springer Berlin Heidelberg, pp. 135–141.

[12] Dussauge, J.-P. and Piponniau, S., 2008, "Shock/boundary-layer interactions: Possible sources of unsteadiness," Journal of Fluids and Structures, **24**(8), pp. 1166–1175.

[13] Touber, E. and Sandham, N. D., 2009, "Large-eddy simulation of low-frequency unsteadiness in a turbulent shock-induced separation bubble," Theoretical and Computational Fluid Dynamics, **23**(2), pp. 79–107.

[14] Bode, C., Przytarski, P. J., Leggett, J., and Sandberg, R. D., 2022, "Highly Resolved Large-Eddy Simulations of a Transonic Compressor Stage Midspan Section Part I: Effect of Inflow Disturbances," *Volume 10D: Turbomachinery — Multidisciplinary Design Approaches, Optimization, and Uncertainty Quantification Turbomachinery General Interest Unsteady Flows in Turbomachinery*, American Society of Mechanical Engineers, doi: 10.1115/gt2022-81673.

[15] Priebe, S., Wilkin, D., Breeze-Stringfellow, A., Mousavi, A., Bhaskaran, R., and d'Aquila, L., 2022, "Large Eddy Simulations of a Transonic Airfoil Cascade," *Volume 10A: Turbomachinery — Axial Flow Fan and Compressor Aerodynamics*, American Society of Mechanical Engineers, doi: 10.1115/gt2022-80683.

[16] Klose, B. F., Morsbach, C., Bergmann, M., Hergt, A., Klinner, J., Grund, S., and Kügeler, E., 2023, "A Numerical Test Rig for Turbomachinery Flows Based on Large Eddy Simulations With a High-Order Discontinuous Galerkin Scheme—Part II: Shock Capturing and Transonic Flows," Journal of Turbomachinery, **146**(2).

[17] Klose, B. F., Munoz Lopez, E. J., Hergt, A., Klinner, J., Bergmann, M., and Morsbach, C., 2023, *Analysis of a Transonic Cascade with Wall-Modeled LES Based on DGSEM*, Springer Nature Switzerland, pp. 157–163.

[18] Wang, Z., Fidkowski, K., Abgrall, R., Bassi, F., Caraeni, D., Cary, A., and Deconinck, H., et al., 2013, "High-order CFD methods: current status and perspective," International Journal for Numerical Methods in Fluids, **72**(8), pp. 811–845.

[19] Kronbichler, M. and Persson, P.-O., eds., 2021, *Efficient High-Order Discretizations for Computational Fluid Dynamics*, Springer International Publishing.

[20] Hindenlang, F. J., Gassner, G. J., and Munz, C.-D., 2014, "Improving the accuracy of discontinuous Galerkin schemes at boundary layers," International Journal for Numerical Methods in Fluids, **75**(6), pp. 385–402.

[21] Gassner, G. J., Winters, A. R., and Kopriva, D. A., 2016, "Split form nodal discontinuous Galerkin schemes with summation-by-parts property for the compressible Euler equations," Journal of Computational Physics, **327**, pp. 39–66.

[22] Winters, A. R., Moura, R. C., Mengaldo, G., Gassner, G. J., Walch, S., Peiro, J., and Sherwin, S. J., 2018, "A comparative study on polynomial dealiasing and split form discontinuous Galerkin schemes for under-resolved turbulence computations," Journal of Computational Physics, **372**, pp. 1–21.

[23] Garai, A., Diosady, L., Murman, S., and Madavan, N., 2015, "DNS of Flow in a Low-Pressure Turbine Cascade Using a Discontinuous-Galerkin Spectral-Element Method," *Volume 2B: Turbomachinery*, American Society of Mechanical Engineers, doi: 10.1115/gt2015-42773.

[24] Bergmann, M., Morsbach, C., Klose, B. F., Ashcroft, G., and Kügeler, E., 2023, "A Numerical Test Rig for Turbomachinery Flows Based on Large Eddy Simulations With a High-Order Discontinuous Galerkin Scheme—Part I: Sliding Interfaces and Unsteady Row Interactions," Journal of Turbomachinery, **146**(2).

[25] Morsbach, C., Bergmann, M., Tosun, A., Klose, B. F., Bechlars, P., and Kügeler, E., 2023, "A Numerical Test Rig for Turbomachinery Flows Based on Large Eddy Simulations With a High-Order Discontinuous Galerkin Scheme—Part III: Secondary Flow Effects," Journal of Turbomachinery, **146**(2).

[26] TEAMAero, 2021, "Towards Effective Flow Control and Mitigation of Shock Effects in Aeronautical Applications," https://h2020-teamaero.eu

[27] Munoz Lopez, E. J., Hergt, A., Klinner, J., Grund, S., Karboujian, J., Flamm, J., and Gümmer, V., 2023, "Investigations of the Unsteady Shock-Boundary Layer Interaction in a Transonic Compressor Cascade," *Volume 13D: Turbomachinery — Multidisciplinary Design Approaches, Optimization, and Uncertainty Quantification; Radial Turbomachinery Aerodynamics; Unsteady Flows in Turbomachinery*, American Society of Mechanical Engineers, doi: 10.1115/gt2023-102622.

[28] Klinner, J., Munoz Lopez, E. J., Hergt, A., and Willert, C., 2023, "High-resolution PIV measurements of the shock boundary layer interaction within a highly loaded transonic compressor cascade," *15th International Symposium on Particle Image Velocimetry {–} ISPIV 2023*, https://elib.dlr.de/197278/

[29] Morsbach, C., 2016, "Reynolds Stress Modelling for Turbomachinery Flow Applications," Ph.D. thesis, Technischen Universität Darmstadt.

[30] Geiser, G., Wellner, J., Kügeler, E., Weber, A., and Moors, A., 2019, "On the Simulation and Spectral Analysis of Unsteady Turbulence and Transition Effects in a Multistage Low Pressure Turbine," Journal of Turbomachinery, **141**(5).

[31] Menter, F., Kuntz, M., and Langtry, R., 2003, "Ten years of Industrial experience with the SST model," *Turbulence, Heat and Mass Transfer 4*, K. Hanjalić, Y. Nagano, and M. Tummers, eds.

[32] Kato, M. and Launder, B. E., 1993, "The Modeling of Turbulent Flow Around Stationary and Vibrating Square Cylinders," *9th Symposium on Turbulent Shear Flows*, pp. 10.4.1–10.4.6.

[33] Langtry, R. B. and Menter, F. R., 2009, "Correlation-Based Transition Modeling for Unstructured Parallelized Computational Fluid Dynamics Codes," AIAA Journal, **47**(12), pp. 2894–2906.

[34] Venkatakrishnan, V., 1993, "On the accuracy of limiters and convergence to steady state solutions," *31st Aerospace Sciences Meeting*, American Institute of Aeronautics and Astronautics, doi: 10.2514/6.1993-880.

[35] Roe, P., 1981, "Approximate Riemann solvers, parameter vectors, and difference schemes," Journal of Computational Physics, **43**(2), pp. 357–372.

[36] Bergmann, M., Gölden, R., and Morsbach, C., 2018, "Numerical investigation of split form nodal discontinuous Galerkin schemes for the implicit LES of a turbulent channel flow," *Proceedings of the 7th European Conference on Computational Fluid Dynamics*.

[37] Bergmann, M., Morsbach, C., and Ashcroft, G., 2020, "Assessment of Split Form Nodal Discontinuous Galerkin Schemes for the LES of a Low Pressure Turbine Profile," *ERCOFTAC Series*, Springer International Publishing, pp. 365–371.

[38] Kopriva, D. A., 2009, *Implementing Spectral Methods for Partial Differential Equations*, Springer Netherlands.

[39] Chandrashekar, P., 2013, "Kinetic Energy Preserving and Entropy Stable Finite Volume Schemes for Compressible Euler and Navier-Stokes Equations," Communications in Computational Physics, **14**(5), pp. 1252–1286.

[40] Bassi, F. and Rebay, S., 1997, "A High-Order Accurate Discontinuous Finite Element Method for the Numerical Solution of the Compressible Navier–Stokes Equations," Journal of Computational Physics, **131**(2), pp. 267–279.

[41] Hennemann, S., Rueda-Ramírez, A. M., Hindenlang, F. J., and Gassner, G. J., 2021, "A provably entropy stable subcell shock capturing approach for high order split form DG for the compressible Euler equations," Journal of Computational Physics, **426**, p. 109935.

[42] Fernandez, P., Nguyen, N.-C., and Peraire, J., 2018, "A physics-based shock capturing method for large-eddy simulation," .

[43] Rueda-Ramírez, A. M., Pazner, W., and Gassner, G. J., 2022, "Subcell limiting strategies for discontinuous Galerkin spectral element methods," Computers & Fluids, p. 105627.

[44] Shu, C.-W. and Osher, S., 1988, "Efficient implementation of essentially non-oscillatory shock-capturing schemes," Journal of Computational Physics, **77**(2), pp. 439–471.

[45] Munoz Lopez, E. J., Hergt, A., Ockenfels, T., Grund, S., and Gümmer, V., 2023, "The Current Gap between Design Optimization and Experiments for Transonic Compressor Blades," International Journal of Turbomachinery, Propulsion and Power, **8**(4), p. 47.

[46] Schlüß, D., Frey, C., and Ashcroft, G., 2016, "Consistent Non-reflecting Boundary Conditions For Both Steady And Unsteady Flow Simulations In Turbomachinery Applications," *ECCOMAS Congress 2016 VII European Congress on Computational Methods in Applied Sciences and Engineering, Crete Island, Greece*.

[47] Geuzaine, C. and Remacle, J.-F., 2009, "Gmsh: A 3-D finite element mesh generator with built-in pre- and post-processing facilities," International Journal for Numerical Methods in Engineering, **79**(11), pp. 1309–1331.

[48] Karypis, G. and Kumar, V., 1998, "A fast and high quality multilevel scheme for partitioning irregular graphs," SIAM JOURNAL ON SCIENTIFIC COMPUTING, **20**(1), pp. 359–392.

[49] Bergmann, M., Morsbach, C., Ashcroft, G., and Kügeler, E., 2021, "Statistical Error Estimation Methods for Engineering-Relevant Quantities From Scale-Resolving Simulations," Journal of Turbomachinery, **144**(3).

[50] Schmidt, O. T. and Colonius, T., 2020, "Guide to Spectral Proper Orthogonal Decomposition," AIAA Journal, **58**(3), pp. 1023–1033.

[51] Morsbach, C., Klose, B. F., Bergmann, M., and Möller, F. M., 2024, "Modal analysis of high-fidelity simulations in turbomachinery," .

List of Figures

List of Tables